Contrasting Spring and Summer Large-Scale Environments Associated with Mesoscale Convective Systems over the U.S. Great Plains

FENGFEI SONG, ZHE FENG, AND L. RUBY LEUNG

Atmospheric Sciences and Global Change Division, Pacific Northwest National Laboratory, Richland, Washington

ROBERT A. HOUZE JR.

Atmospheric Sciences and Global Change Division, Pacific Northwest National Laboratory, Richland, and Department of Atmospheric Sciences, University of Washington, Seattle, Washington

JINGYU WANG AND JOSEPH HARDIN

Atmospheric Sciences and Global Change Division, Pacific Northwest National Laboratory, Richland, Washington

CAMERON R. HOMEYER

School of Meteorology, University of Oklahoma, Norman, Oklahoma

(Manuscript received 7 December 2018, in final form 21 June 2019)

ABSTRACT

Mesoscale convective systems (MCSs) are frequently observed over the U.S. Great Plains during boreal spring and summer. Here, four types of synoptically favorable environments for spring MCSs and two types each of synoptically favorable and unfavorable environments for summer MCSs are identified using self-organizing maps (SOMs) with inputs from observational data. During spring, frontal systems providing a lifting mechanism and an enhanced Great Plains low-level jet (GPLLJ) providing anomalous moisture are important features identified by SOM analysis for creating favorable dynamical and thermodynamic environments for MCS development. During summer, the composite MCS environment shows small positive convective available potential energy (CAPE) and convective inhibition (CIN) anomalies, which are in stark contrast with the large positive CAPE and negative CIN anomalies in spring. This contrast suggests that summer convection may occur even with weak large-scale dynamical and thermodynamic perturbations so MCSs may be inherently less predictable in summer. The two synoptically favorable environments identified in summer have frontal characteristics and an enhanced GPLLJ, but both shift north compared to spring. The two synoptically unfavorable environments feature enhanced upper-level ridges, but differ in the strength of the GPLLJ. In both seasons, MCS precipitation amount, area, and rate are much larger in the frontal-related MCSs than in nonfrontal MCSs. A large-scale index constructed using pattern correlation between large-scale environments and the synoptically favorable SOM types is found to be skillful for estimating MCS number, precipitation rate, and area in spring, but its explanatory power decreases significantly in summer. The low predictability of summer MCSs deserves further investigation in the future.

1. Introduction

Mesoscale convective systems (MCSs), the largest convective storms, develop and become organized when convection aggregates and induces mesoscale circulation features to become significantly different from isolated convection events (e.g., Zipser 1982; Fritsch and Forbes 2001; Houze 2004, 2018). The U.S. Great Plains, east of the Rocky Mountains, is home to some of the most intense MCSs on Earth. MCSs are very active over the Great Plains during boreal spring and summer, producing ~30%–70% of total rainfall (Feng et al. 2016; Fritsch et al. 1986; Nesbitt et al. 2006; Haberlie and Ashley 2019) and ~60%–75% of extreme rainfall

Supplemental information related to this paper is available at the Journals Online website: https://doi.org/10.1175/JCLI-D-18-0839.s1.

Corresponding author: Fengfei Song, fengfei.song@pnnl.gov

DOI: 10.1175/JCLI-D-18-0839.1

(Maddox et al. 1979; Schumacher and Johnson 2005, 2006) in the region. Hence, better understanding of MCSs is important for improving precipitation prediction over the Great Plains.

The role of large-scale environments in the initiation and development of MCSs over the Great Plains has been extensively studied (e.g., Maddox 1983; Anderson and Arritt 1998; Coniglio et al. 2004, 2010). Based on composites of sounding data around the MCSs, Maddox (1983) found that intense MCSs are often initiated ahead of large-scale troughs in the westerlies, where large-scale upward motion occurs. Coniglio et al. (2010) compared the large-scale environments between rapidly and slowly developing MCSs and between the long- and short-lived MCSs over the Great Plains and found differences in the environments, such as the Great Plains low-level jet (GPLLJ), instability, frontal zone, moisture depth, vertical wind shear, and potential vorticity. Peters and Schumacher (2014) suggested that heavy-rain-producing MCSs over the Great Plains exhibit distinct large-scale environments for warm-season versus synoptic storms. They found that synoptic-type MCSs often occur downstream of an upper-level trough, while warm-season-type MCSs often occur near the entrance region of an upper-level jet. Yang et al. (2017) also found that large-scale environments including the GPLLJ and upper-level trough are more prominent at the time of MCS initiation for long-lived than short-lived MCSs. Although previous studies obtained large-scale environments for certain types of MCSs, the relative importance of different large-scale environments has not been quantified. Furthermore, while many studies focused on the favorable large-scale environments for different types of MCSs, some studies noted that MCSs over the Great Plains can occur under weak synoptic forcing or unfavorable large-scale environment, especially during the summertime (e.g., Johns 1982, 1984, 1993; Wang et al. 2011a,b; Pokharel et al. 2019). In the case of weak forcing, MCSs occur in northwesterly flow associated with a high-pressure ridge to the west and a low-pressure trough to the east. Although large-scale upward motion is suppressed or weak under such large-scale environments, a shortwave perturbation embedded in the large-scale flow may nevertheless support convection. It is still unclear to what extent MCSs over the Great Plains are associated with favorable or unfavorable large-scale environments. Hence, one goal of this study is to systematically identify the extent to which MCSs over the Great Plains are associated with particular large-scale environments during the warm season, especially contrasting springtime versus summertime. To this end, we have conducted self-organizing map (SOM; Kohonen 2001) analysis to characterize the large-scale environments associated with MCSs observed during a 10-yr period (2004–13). This methodology allows us to identify different kinds of large-scale environments associated with MCSs, which may be either favorable or unfavorable. Furthermore, we quantified the predictive power of the synoptically favorable environments during MCS initiation for different aspects of MCSs during their life cycle. Isolating the large-scale environments at initiation minimizes the effect of feedback from the MCSs to the large-scale environments (e.g., Ninomiya 1971; Maddox 1980; Fritsch and Maddox 1981; Perkey and Maddox 1985; Smull and Augustine 1993; Keyser and Johnson 1984; Fritsch et al. 1994; Wolf and Johnson 1995; Stensrud 1996; Fritsch et al. 1994; Houze 2004, 2018; Yang et al. 2017; Feng et al. 2018), which can mask causality or predictability. We developed a large-scale index (LI) from the SOM types to estimate the occurrence and characteristics of MCSs during 2014–16 We find that the LI can explain a significant fraction of MCSs during spring but there is lower skill during summer.

The remainder of this paper is organized as follows: section 2 introduces the MCS observations, reanalysis datasets, and SOM method. Section 3 discusses the main results, which include the common features and different types of large-scale environments associated with MCSs, the MCS characteristics associated with different types of large-scale environments, and prediction of MCS characteristics based on the large-scale environments at initiation. Section 4 provides a summary and discusses limitations of the study and future work.

2. MCS observations and analysis methods

a. MCS identification and tracking

In this study, we make use of three operational datasets to identify and track MCSs in the U.S. Great Plains region: 1) the global merged geostationary satellite infrared brightness temperature (T_b) dataset (Janowiak et al. 2017) produced by National Oceanic and Atmospheric Administration (NOAA) Climate Prediction Center and archived at NASA Goddard Earth Sciences Data and Information Services Center (GES DISC); 2) a three-dimensional mosaic National Weather Service Next-Generation Radar (NEXRAD) radar reflectivity dataset known as GridRad (Homeyer and Bowman 2017; Cooney et al. 2018); and 3) the Stage IV multisensor hourly precipitation dataset produced by the 12 River Forecast Centers in the continental United States (CONUS) (Lin 2011). The satellite T_b data are available at 30 min and ~4 km,

the GridRad reflectivity data are provided at hourly and ~2 km in the horizontal and 1 km in the vertical, and the Stage IV precipitation data are available at hourly and ~4 km. Both the GridRad and Stage IV data are regridded onto the satellite 4-km grid using the Earth System Modeling Framework (ESMF) regridding software (https://www.ncl.ucar.edu/Applications/ESMF.shtml).

All three datasets cover a common 13-yr period (2004–16), so we focus on this period for MCS tracking covering a majority of the continental United States east of the Rocky Mountains within 25°–50°N, 110°–70°W. A recently developed MCS tracking algorithm called the Flexible Object Tracker (FLEXTRKR) is used to identify and track long-lived and intense MCSs (Feng et al. 2018). The method first makes use of satellite T_b data to track large cold cloud systems (CCSs) associated with deep convective clouds, and subsequently uses the 3D radar reflectivity data to identify large precipitation features (PFs) that contain intense convection. In this study, an MCS is defined as a large CCS (area $>6 \times 10^4$ km^2) containing a PF with major axis length >100 km and convective radar reflectivity >45 dBZ, and persisting for at least 6 h. MCSs in the study domain are tracked from March to October each year, and we focus on MCSs occurring over the Great Plains (25°–50°N, 90°–105°W) during March–May (MAM) and June–August (JJA). More details about the MCS spatiotemporal characteristics revealed from the 13-yr MCS database can be found in Feng et al. (2019).

For each tracked MCS, FLEXTRKR defines four life cycle stages: convective initiation, MCS genesis, mature, and dissipation stages. Convective initiation occurs during the first hour a CCS is detected in the satellite T_b data that eventually becomes an MCS. MCS genesis occurs during the first hour after the major axis length of a convective feature exceeds 100 km. The mature stage is defined as the period when the convective feature maintains its major axis length of 100 km and the stratiform rain area exceeds its mean value averaged over the entire duration of the MCS. The dissipate stage occurs when the convective feature is less than 100 km wide or the stratiform rain area decreases to below the mean value of the MCS. A small fraction of MCSs (~10%) do not have convective features larger than 100 km and hence not all life cycle stages can be defined. In this study, we only select MCSs that go through all the life cycle stages defined above. FLEXTRKR also provides many statistical properties of each tracked MCS, including its duration, precipitation feature area, mean precipitation rate, and accumulated precipitation amount. These MCS properties are used in section 3d to construct the LI and evaluate its predictive power.

b. MCS large-scale environments

We separate the MCS database into two periods: 2004–13 is used to train the SOM to identify different types of large-scale environments and 2014–16 is used to examine the predictive power of the large-scale environments on MCSs. During 2004–13, we identify a total of 494 and 812 MCSs in spring and summer over the Great Plains, respectively. During 2014–16, there are 176 and 271 MCSs in spring and summer, respectively. Long-lived and intense MCSs have significant feedbacks to the large-scale environments through their top-heavy diabatic heating profiles that generate potential vorticity (e.g., Ninomiya 1971; Maddox 1980; Fritsch and Maddox 1981; Perkey and Maddox 1985; Smull and Augustine 1993; Keyser and Johnson 1984; Wolf and Johnson 1995; Stensrud 1996; Yang et al. 2017; Feng et al. 2018). To study the large-scale environment conducive to MCS development, only the large-scale environments at the time of MCS initiation are used in our analysis to minimize the effects of MCS feedback to the large-scale environment. For the same reason, we adopt the fixed-space (Eulerian) rather than the MCS-relative (Lagrangian) compositing method to analyze the persistent large-scale features while smoothing out recurrent MCS-following mesoscale features (Augustine and Howard 1991; Anderson and Arritt 1998).

We use 3-hourly data of zonal and meridional winds (925, 500, 200 hPa), specific humidity (925 and 500 hPa), vertical velocity (500 hPa), geopotential height (200 hPa), convective available potential energy (CAPE), and convective inhibition (CIN) from the North American Regional Reanalysis (NARR) dataset (Mesinger et al. 2006) to represent the large-scale environments. Gensini et al. (2014) noted that CAPE is biased high in NARR based on analysis of more than 100 000 soundings regardless of whether there is convection. However, King and Kennedy (2019) found that the CAPE in NARR is most comparable with the observations among several reanalysis datasets when they focused on the convective environments. Hence, biases in the thermodynamic variables in NARR may have limited effects on the composite of CAPE and CIN when MCSs occur. For each MCS identified by the tracking method, we include the large-scale environments at or 1–2 h prior to the initiation moments of MCSs to reconcile the different temporal resolutions of the MCSs data (1 hourly) and reanalysis data (3 hourly). For example, for a given MCS initiated between 0000 and 0200 UTC, the large-scale environments at 0000 UTC are selected. We also use the 6-hourly ERA-Interim dataset

(Dee et al. 2011) to conduct the same analysis to confirm that the results are not sensitive to the reanalysis datasets (see Figs. S1 and S2 in the online supplemental material for spring and summer, respectively).

c. SOM analysis

We conduct an analysis using SOM to identify different types of large-scale environments associated with MCSs over the Great Plains. SOM is a clustering method developed in the field of artificial neural networks and has been widely used in atmospheric science (e.g., Reusch et al. 2007; Lee et al. 2011; Bao and Wallace 2015; Wang et al. 2019). Similar to other clustering methods, SOM projects high-dimensional input data onto a low-dimensional (here two-dimensional) space. An open-source SOM Python package (SOMPY; https://github.com/sevamoo/SOMPY) is used in this study. Before the machine-learning process, the initiation nodes are assigned by randomly or more efficiently selecting them from the leading empirical orthogonal functions (EOFs). Then we calculate the Euclidean distance between each input pattern and the initiation nodes to begin an iterative procedure, which is also called "training" of SOM. The best-matching node or the "winning" node is the one with the smallest distance between the initiation nodes and the input pattern. Finally, the winning node and the neighborhood nodes around the winner are all updated to adjust themselves toward the input pattern. Since this process is iterated and fine-tuned, the nodes are self-organizing. We call the final SOM nodes the large-scale environment types associated with MCSs. Here, we use the zonal and meridional winds at three levels (925, 500, and 200 hPa) and the specific humidity at two levels (925 and 500 hPa) over the domain 20°–55°N, 70°–110°W during MAM and JJA in 2004–13 to construct a training dataset for spring and summer, respectively. All variables are normalized by removing their time mean and divided by their standard deviation over all times with MCS initiation. The cosine-latitude weighting is adopted when the spatial dimensions of the variables are collapsed into a single dimension. We tested a slightly larger domain (15°–60°N, 60°–130°W) and smaller domain (25°–50°N, 90°–105°W) to confirm that our main results are not affected by the domain size. We also tested the use of more variables, such as including CAPE and CIN, and the results are also found to be quite similar. The choice of how many SOM nodes to prescribe is a trade-off between distinctiveness and robustness. As shown in Fig. S3 and Fig. S4 for six nodes of the SOM analysis for spring and summer, respectively, it is apparent that some nodes are still redundant. Here, we choose four nodes for both spring and summer, which allow distinct large-scale environments to be captured while minimizing redundant nodes that are similar.

3. Results

a. Common features of large-scale environments associated with MCSs

The large-scale environments over the Great Plains share some similarity as well as distinct features during boreal spring (MAM) and summer (JJA). In both seasons, low-level southerly wind, namely the GPLLJ, transports abundant water vapor from the warm Gulf of Mexico to the Great Plains, resulting in a meridional moisture gradient between the northern and southern Great Plains and a zonal moisture gradient between the Rocky Mountains and the Great Plains (Figs. 1a,b). Despite a slightly weaker GPLLJ, the moisture transport during summer is comparable to spring because the low-level moisture during summer is much higher than during spring due to the warmer temperature. At the upper levels, the Great Plains is located ahead of a large-scale trough during MAM, which is favorable for upward motion to develop (Fig. 1c). In contrast, the region is occupied by a high-pressure ridge and westerly flow during summer (Fig. 1d). When MCSs occur during spring, low-level moisture transport is substantially enhanced via a stronger GPLLJ and a positive moisture anomaly maximum is found over the Great Plains (Fig. 1e). But in summer, the GPLLJ and moisture anomalies associated with MCSs are not significant (Fig. 1f). During spring when MCSs occur, there is a negative and positive eddy geopotential height anomaly at the upper-level west and east of Great Plains (Fig. 1g), respectively, suggestive of a stronger trough and ridge that favor stronger large-scale upward motion. In summer, the pair of upper-level negative and positive geopotential height anomaly becomes much weaker and exhibits a northeast–southwest orientation that induces anomalous southwesterly wind over the Great Plains (Fig. 1h).

We further examine the large-scale dynamical and thermodynamic factors associated with MCSs over the Great Plains during spring and summer (Fig. 2). In spring, anomalous low-level convergence and midlevel upward motion are prevalent over the Great Plains when MCSs occur (Figs. 2a,c). These conditions are also found in summer but the anomalies are much weaker especially for the midlevel upward motion, and they occupy smaller areas and are shifted northward corresponding to the northward shift of MCS occurrence in summer relative to spring (Figs. 2b,d). In the thermodynamic fields, the northward shift of CAPE and CIN is also evident in

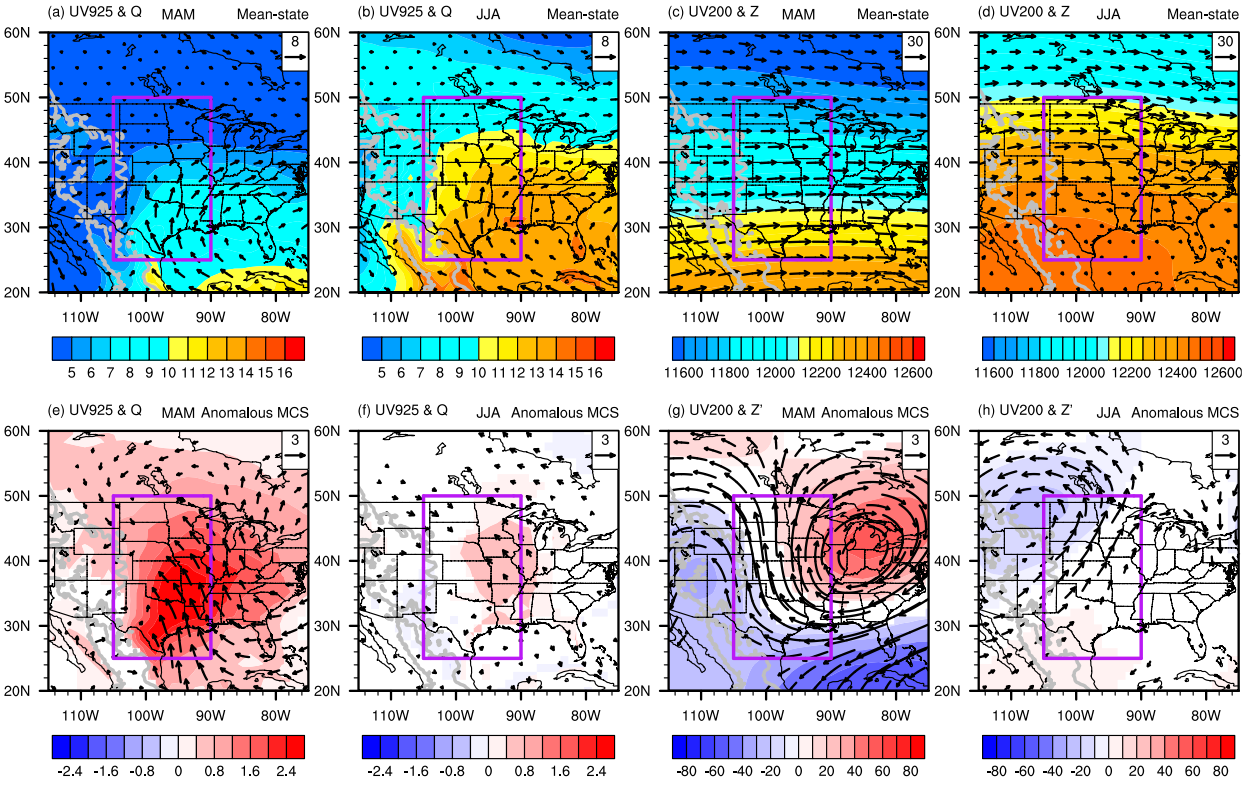

FIG. 1. (top) Climatology of (a),(b) 925-hPa winds (vectors; m s^{-1}) and specific humidity (shading; g kg^{-1}) and (c),(d) 200-hPa winds (vectors; m s^{-1}) and geopotential height (shading; gpm), and (bottom) the composite anomalies of (e),(f) 925-hPa wind (vectors; m s^{-1}) and specific humidity (shading; g kg^{-1}) and (g),(h) 200-hPa winds (vectors; m s^{-1}) and eddy geopotential height (shading; gpm) for MCSs occurring in (a),(c),(e),(g) MAM and (b),(d),(f),(h) JJA. The gray contour shows elevation higher than 1500 m based on the TBASE data. The purple box shows the location of the U.S. Great Plains (25°–50°N, 90°–105°W). In (e) and (f), specific humidity anomalies are shown when they are significant at the 5% level; wind vectors are shown when either the zonal or meridional wind anomalies are significant at the 5% level.

summer compared to spring (Figs. 2e–h). The CAPE anomaly is much stronger during spring than summer, consistent with the seasonal difference of the low-level moisture anomalies (Figs. 1e,f). In contrast to the magnitude difference in the variables discussed so far, there is a sign difference in CIN between the two seasons (Figs. 2g,h). In spring, the CIN anomaly is negative in the Great Plains, but it changes to positive in summer. The change in the CIN anomaly means that during spring, the thermodynamics of the boundary layer suppresses convective development, so stronger dynamical lifting (e.g., low-level convergence) and low-level moistening are needed to destabilize the boundary layer. But during summer, the boundary layer is unstable (positive CIN), so weak dynamical and thermodynamic large-scale perturbations are enough to trigger convection.

b. *Different types of large-scale environments associated with MCSs*

The composites of large-scale environments associated with all MCS initiation moments shown in Figs. 1 and 2 suggest that the large-scale forcing of MCSs over the Great Plains during boreal spring is much stronger than that during summer. Here we study different types of large-scale environments associated with the large number of MCSs observed during 2004–13. Using SOM analysis, we identify four types of large-scale environments associated with MCSs over the Great Plains for each season during spring and summer.

During spring, four types of large-scale environments that support MCSs are distinct. In the first type (type 1; Figs. 3a and 4a), anomalous southerly winds dominate most of the Great Plains, with weak northerly winds in the northwestern edge. Between the northerly and southerly winds is a synoptic front with large moisture gradient (dry northwest–wet southeast). There is also an enhanced moisture gradient between the Great Plains and Rocky Mountains in type 1, compared to all MCSs mean (Fig. 1e). Most MCSs initiate on the moist side of the front but are broadly distributed in the Great Plains due to the penetration of the GPLLJ into the northern Great Plains. In type 2 (Figs. 3b and 4b), anomalous

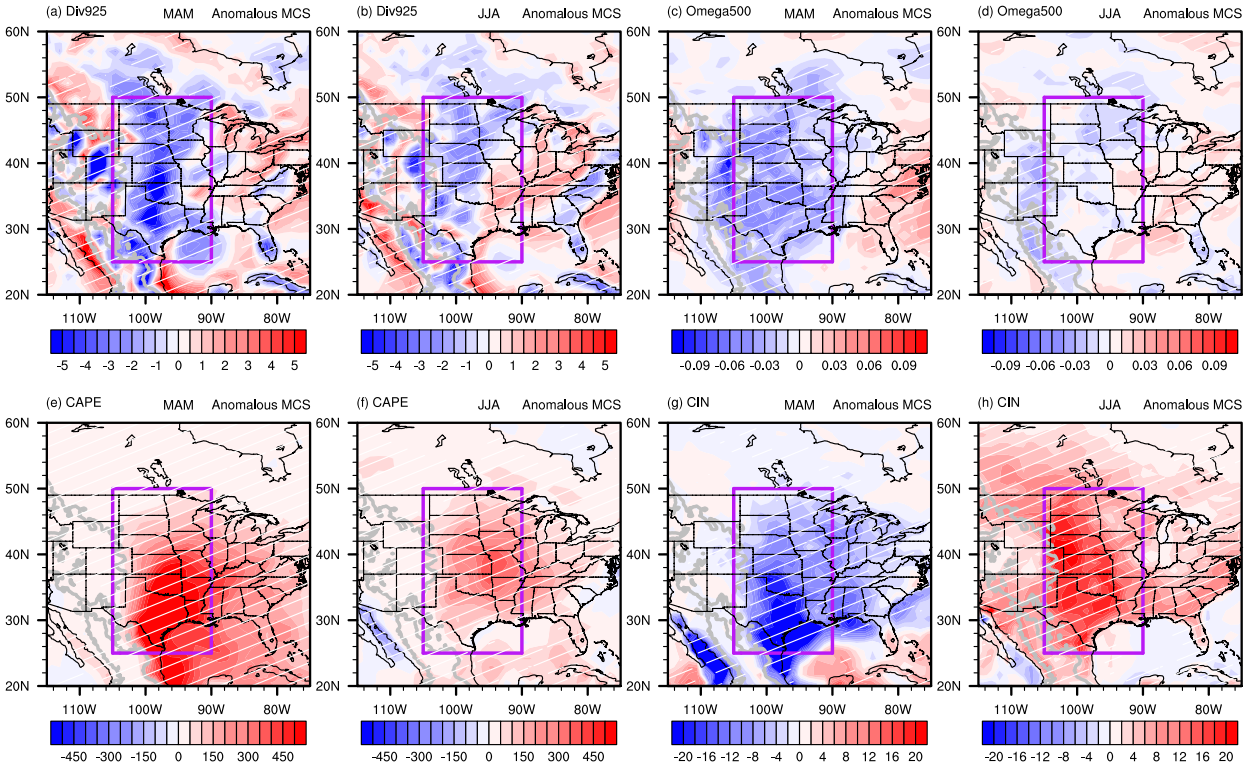

FIG. 2. As in Fig. 1, but for composite anomalies of (a),(b) 925-hPa divergence ($10^{-6}\,s^{-1}$), (c),(d) 500-hPa vertical velocity ($Pa\,s^{-1}$), (e),(f) CAPE ($J\,kg^{-1}$), and (g),(h) CIN ($J\,kg^{-1}$) for MCSs occurring in (a),(c),(e),(g) MAM and (b),(d),(f),(h) JJA. The hatched regions indicate the anomalies are significant at the 5% level.

southeasterly instead of southerly winds occupy almost the entire domain, creating a sharp moisture gradient along the Rocky Mountains. Also, MCSs tend to initiate more on the western side of the Great Plains. Strong low-level jets in these two types produce moisture greater than $4\,g\,kg^{-1}$ in the whole Great Plains (Fig. 3). These two types correspond to MCSs that are widely distributed in the whole domain, which are known to be the typical spring MCS environments in many previous studies (e.g., Maddox 1983; Coniglio et al. 2004, 2010; Peters and Schumacher 2014). Type 3 (Figs. 3c and 4c) also corresponds to a synoptic front but, different from type 1, the front is located more southeastward. The synoptic front structure is found by Coniglio et al. (2010) as a typical environment that supports long-lived MCSs. Type 3 also corresponds to the largest west–east gradient in moisture anomaly, resembling a dryline commonly seen over the Great Plains (Hoch and Markowski 2005). Notably the anomalous northerly–southerly winds are of comparable strength, coinciding with dry and wet anomalies, respectively. Hence, type 3 features conditions of a more distinct moisture front compared to types 1 and 2. Similar to type 1, most MCSs initiate on the moist side of the front, but the initiation evidently concentrates more along the frontal zone where the moisture gradient is sharp rather than spread out more broadly in the other types. The last node (type 4; Figs. 3d and 4d) features the northern Great Plains ahead of a mid-/upper-level ridge while the southern Great Plains is collocated with a midlevel ridge. At the same time, a low-level-jet moisture transport, with a weak anomalous cyclonic circulation, is confined primarily to the southern Great Plains, producing a positive moisture anomaly center in Texas. This type resembles the zonal pattern defined in Coniglio et al. (2004). In this type, most MCSs initiate over the southern Great Plains. Types 3 and 4 preferentially occur more during April than the other two months.

These four types of large-scale environments during spring also differ substantially in the middle and upper levels (Fig. 5). In both types 1 and type 3, there is an anomalous upper-level anticyclone east of the Great Plains and an anomalous cyclone west of the Great Plains (Figs. 5a,c), so the Great Plains is located ahead of the upper-level trough (Figs. 3a,c). Similar to the low-level circulation, the pair of cyclone and anticyclone is also located more southeastward in type 3 compared to type 1. There is a strong midlevel upward motion in

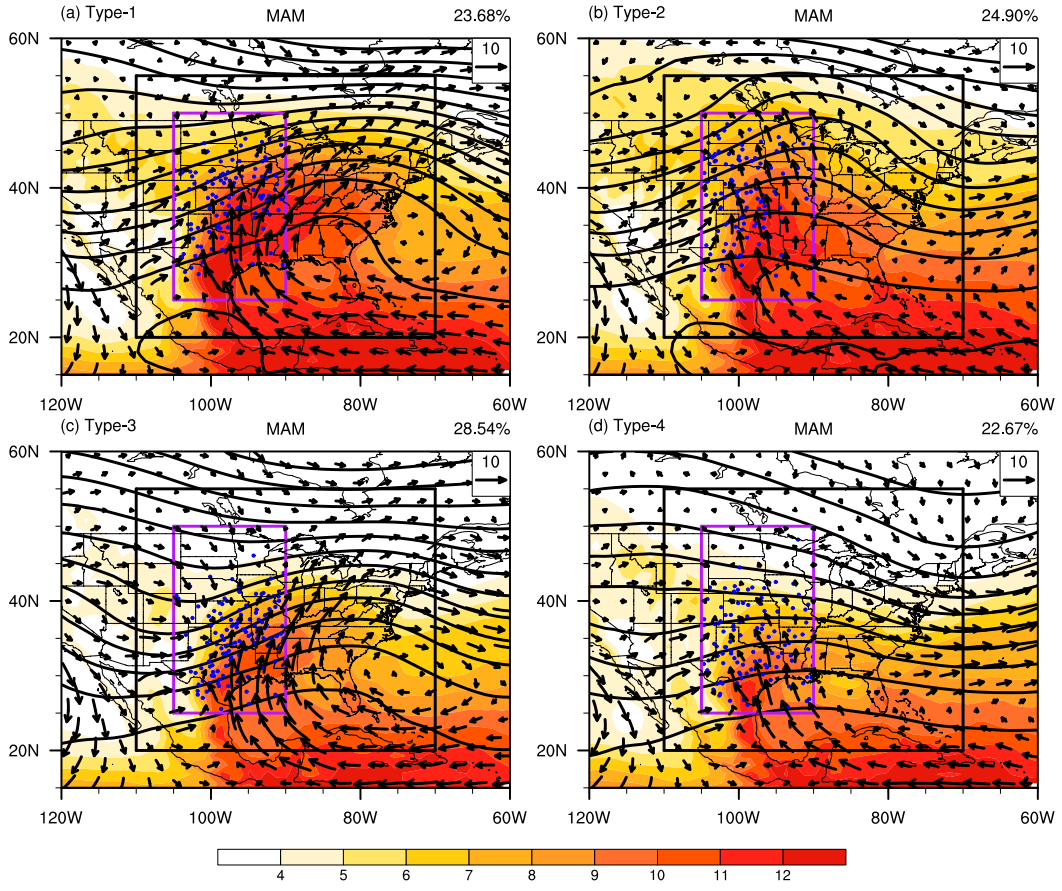

FIG. 3. Composites of 925-hPa winds (vectors; $m\,s^{-1}$), specific humidity (shading; $g\,kg^{-1}$), and 500-hPa geopotential height (contour; gpm) during MAM in four nodes based on SOM analysis. The purple and black boxes indicate the locations of the MCS and SOM analysis domains, respectively. The blue dots denote the location of MCS initiation in each node. The percentage in the upper-right corner indicates the occurrence frequency of each node.

almost the entire Great Plains between the cyclone and anticyclone in these two types of environment. The pair of cyclone and anticyclone is more compact in type 3 than type 1, implying a shorter wavelength in type 3. Consistently, the upward motion occupies a smaller region but has a stronger magnitude in type 3 than type 1. In type 2, the Great Plains is occupied by an upper-level ridge, with the ridge line dividing the region into two parts, corresponding to midlevel upward motion to the northwest and downward motion to the southeast (Figs. 3b and 5b). This also explains why the MCSs in type 2 are mostly confined to the northwestern side of the Great Plains. In type 4, the southern Great Plains is located ahead of a trough, with an anomalous upper-level anticyclone to the east, which is not statistically significant and thus does not show up in Fig. 5d, and an anomalous cyclone to the west, respectively (Figs. 3d and 5d). However, the anomalous anticyclone and cyclone are much weaker compared to that of type 1 and type 3. Consistently, the upward motion and MCS initiation is also more confined to the southern Great Plains.

Similar to Figs. 3 and 4, Figs. 6 and 7 show four types of low-level and middle-level large-scale environments associated with MCSs but for summer. The large-scale environment patterns are substantially different from spring. Type 1 in summer also has a synoptic front, similar to type 3 in spring, but the front extends farther northward (Figs. 6a and 7a) into the northern Great Plains. In this type, there is no preference for MCSs to initiate on the moist side of the front and the initiation locations are more widely distributed over the entire Great Plains compared to type 3 in spring. Moisture availability is likely not a strong constraint on MCS initiation during summer because of the moisture abundance so MCS initiation is not as confined to the moist frontal zone as in type 3 in spring. This type has much higher frequency during June and August than

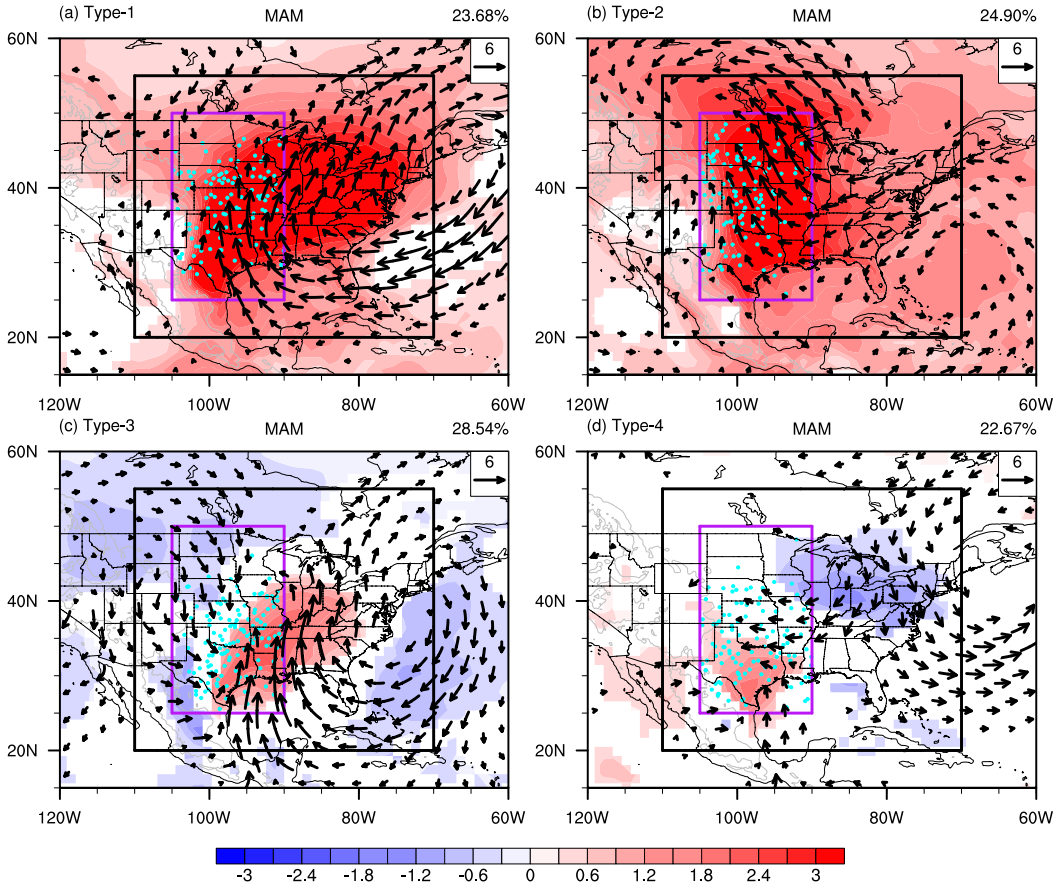

FIG. 4. Composite anomalies of 925-hPa winds (vectors; m s^{-1}) and specific humidity (shading; g kg^{-1}) during MAM in each type of large-scale environment determined by the SOM analysis. The anomalies are relative to all times during MAM. The purple and black boxes indicate the boundaries of MCS initiation over the Great Plains (25°–50°N, 90°–105°W) and the SOM analysis domain (20°–55°N, 70°–110°W), respectively. The cyan dots denote the location of MCS initiation. The percentage in the upper-right corner indicates the percentage of occurrence of each environment type. The gray contour shows elevation higher than 1500 m based on the TBASE data. Specific humidity anomalies are shown when they are significant at the 5% level; wind vectors are shown when either the zonal or meridional wind anomalies are significant at the 5% level.

July. Type 2 corresponds to a strengthened GPLLJ converging in the northern Great Plains, with a moisture anomaly center over there (Fig. 7b). The southern Great Plains is influenced by the westward extension of the North Atlantic subtropical high in the midlevel (Fig. 6b). Hence, most MCSs occur in the northern Great Plains and this type occurs more during July and August when the subtropical high is most westward extended. Type 3 also exhibits a strengthened GPLLJ in the northern Great Plains but the anomalous southerly wind is more southeast–northwest oriented, collocating with the positive moisture anomaly (Fig. 7c). This type tends to occur more during July and August. Type 4 exhibits a weakened GPLLJ with anomalous northeasterly wind and deficient moisture in the entire Great Plains. This type is most frequent during June. In both type 3 and type 4, the relationship between the large-scale environments and MCS occurrences is less clear, although MCS initiation appears to concentrate more in regions with positive (type 3) and zero (type 4) moisture anomalies. In the middle level, Great Plains are ahead of a ridge in both type 3 and type 4 (Figs. 6c,d).

The middle- and upper-level large-scale environments associated with MCS initiation during summer are further investigated in Fig. 8. In type 1, the pattern noticeably resembles type 3 in spring (Fig. 5c), with an anomalous cyclone to the west and anomalous anticyclone to the east of the Great Plains (Fig. 8a). Similar to the low-level front, the cyclone and anticyclone pair is also located farther north in summer compared to spring. In such configuration, midlevel large-scale

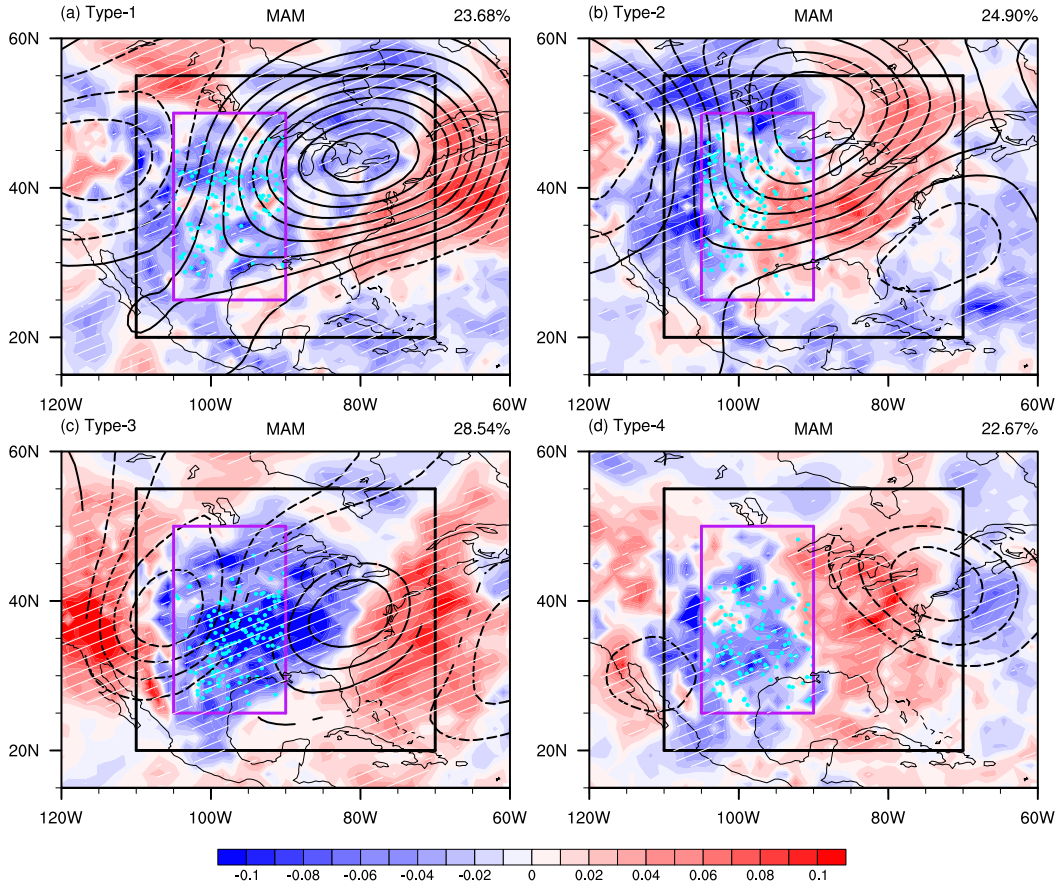

FIG. 5. As in Fig. 4, but for the anomalies of 500-hPa vertical velocity (shading; Pa s^{-1}) and 200-hPa eddy geopotential height anomaly (contour: gpm). The solid (dashed) contours indicate positive (negative) eddy geopotential height anomaly with a contour interval of 20 gpm. The hatched regions indicate where vertical velocity anomalies are significant at the 5% level. Geopotential height anomalies are shown when they are significant at the 5% level.

upward motion dominates over the Great Plains, favoring MCS occurrence. In type 2, there is a northeast–southwest-oriented anticyclone over the northern Great Plains, with a cyclone to the northwest of the Great Plains. Hence, the northern Great Plains is dominated by large-scale upward motion, and the southern Great Plains is occupied by large-scale downward motion. Therefore, type 2 favors MCS development in the northern Great Plains. In contrast to type 1 with a strong cyclone over the Rocky Mountains, there is a weak anticyclone over the mountains and a strong cyclone in northeastern CONUS in type 3 (Fig. 8c). Type 4 also features a pattern opposite to type 2, with a cyclonic anomaly over the Great Plains and an anticyclonic anomaly northwest of the Great Plains (Fig. 8d). Combined with the mean state shown in Fig. 1d, it is evident that the Great Plains is located ahead of a ridge in both type 3 and type 4, with northwesterly winds blowing across the Great Plains (Figs. 6c,d). Although there are scattered areas of upward motion where MCSs are initiated in types 3 and 4, the upward motions are not as organized as shown in types 1 and 2. As pointed out in previous studies (Johns 1982, 1984, 1993; Wang et al. 2011a,b), the presence of a large-scale upper-level ridge similar to that of types 3 and 4 is not favorable for MCSs to develop as it suppresses upward motions. However, smaller-scale perturbations such as middle-tropospheric shortwave forcing may support MCS initiation (Wang et al. 2011a,b; Pokharel et al. 2019). To further confirm this possibility, we calculate the 500-hPa vertical velocity at the moment when an MCS is initiated in a $5° \times 5°$ box centered at the MCS initiation location. We found that 80.4% and 73.6% of MCSs occur with an upward motion averaged over the $5° \times 5°$ box in type 3 and type 4, respectively. Hence, MCS initiations in type 3 and type 4 are most likely triggered by perturbations that are smaller than the synoptic-scale, such as the midtropospheric (e.g., 600 hPa)

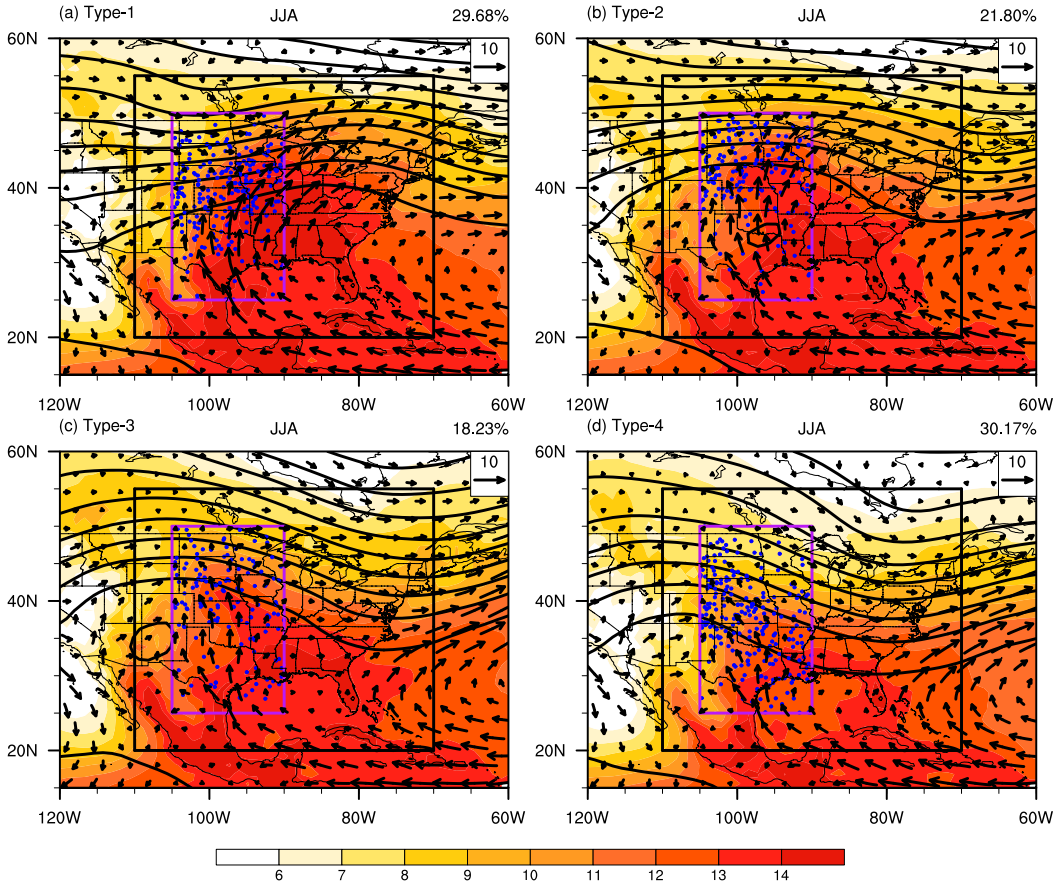

FIG. 6. As in Fig. 3, but for JJA.

perturbations suggested by Wang et al. (2011a,b), or a host of possible local circulations.

c. *MCS characteristics associated with different types of large-scale environments*

The SOM analysis suggests that there are four types of synoptically favorable environments for MCSs in spring, but in summer only two types are synoptically favorable (type 1 and type 2) while the other two types are not synoptically favorable environments for MCSs (type 3 and type 4). What are the MCS characteristics associated with the different types of large-scale environments? Figure 9 shows the diurnal cycle, life cycle stages, and duration of MCSs for each type of large-scale environment in spring and summer. For both seasons, MCSs initiate more often in the early afternoon, with a maximum frequency around 1500 LT and minimum at late night (black line in Figs. 9a and 9b). All environment types follow a similar diurnal cycle, but also exhibit some differences. Type 1 in spring shows the strongest diurnal cycle, with the largest occurrence contrast between afternoon and late night. Considering the life cycle of MCSs in both spring and summer, MCSs generally spend the least amount of time at the initiation stage (~5%) and approximately the same amount of time in the other three stages (~25%–35%; Figs. 9c and 9d). For the frontal-related MCSs in spring (types 1 and 3), they spend more time in the mature stages (i.e., when the stratiform rain area is large) and less time in the dissipation stage, compared to the other two types (Fig. 9c). In summer, the synoptic-related MCSs (types 1 and 2) also spend more time in the mature stage and less time in the dissipation stage than the non-synoptic-related MCSs (types 3 and 4). These results suggest that synoptic-scale forcing tends to support larger MCSs with more pronounced convective features and more expansive stratiform rain area. The duration of MCSs peaks at 18 and 14 h in spring and summer, respectively (black lines in Figs. 9e and 9f). For MCSs in type 1 and type 2 in spring, which are related to the enhanced GPLLJ in the northern Great Plains, the duration also peaks at 18 h, but it is shorter than the other two types (22 h) with MCSs occurring in the southern Great Plains (Fig. 9e). This is expected because the mean background

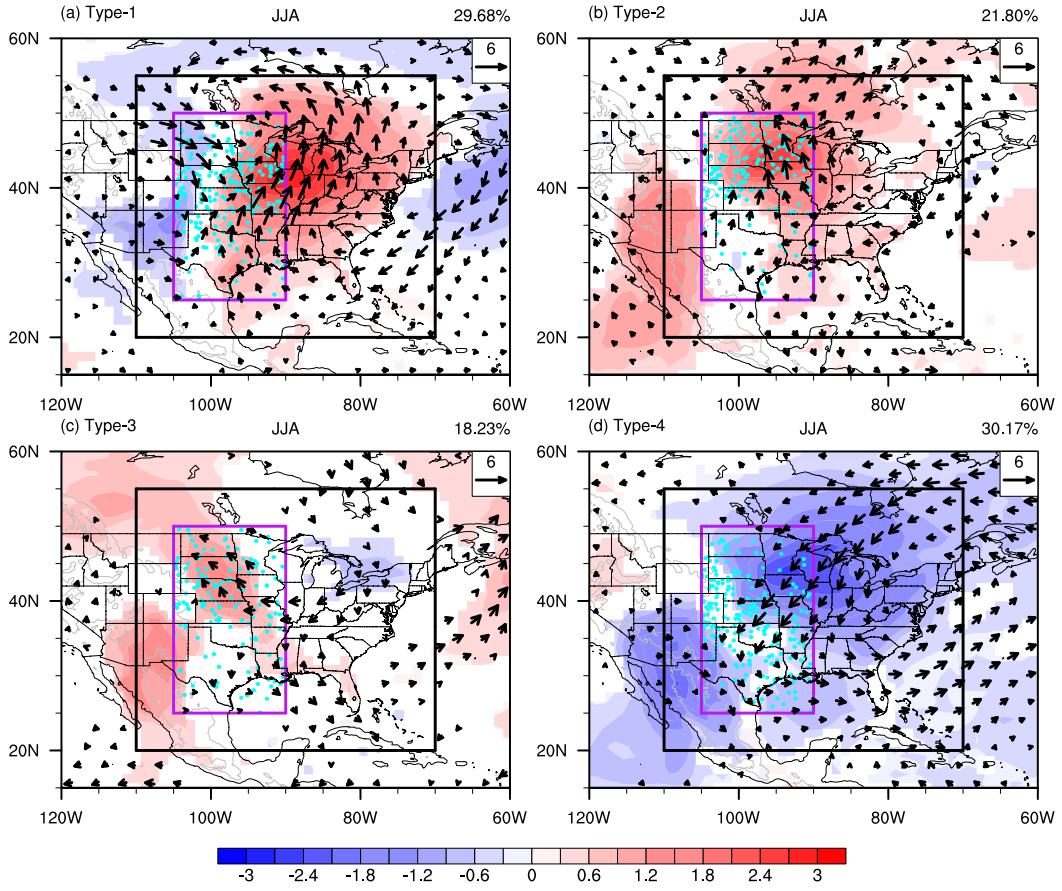

FIG. 7. As in Fig. 4, but for JJA.

moisture in the northern Great Plains is much smaller than the southern Great Plains during spring (Fig. 1a). For summer, the non-synoptic-related MCSs (types 3 and 4) often last longer than the synoptic-related MCSs (types 1 and 2), especially for type 4 (Fig. 9f). This suggests the summertime large-scale environments have less control over the MCS longevity than that in springtime.

MCSs often produce well over 50% of total rainfall in a large area over the Great Plains (Feng et al. 2019). Figure 10 shows the probability distribution of the mean MCS precipitation rate, precipitation area, and precipitation amount for each type of large-scale environment during spring and summer. Generally, the frontal-related types (types 1 and 3) in spring have higher precipitation rate and precipitation area than the other two types (Figs. 10a,b). Hence, MCSs of type 1 and type 3 generate more precipitation amount during their lifetime than the other two types (Fig. 10c). During summer, precipitation rate of the frontal-related type (type 1) is slightly larger and the difference among the other three types is quite small (Fig. 10d). The frontal-related MCSs (type 1) also exhibit much larger precipitation area than the other three types (Fig. 10e), resulting in the largest total precipitation amount (Fig. 10f). The larger precipitation rate, area, and amount in the front-related MCSs may be due to the higher and more spatially extensive moisture and stronger lifting.

d. Estimating MCS characteristics based on the large-scale environments

Using SOM analysis, we obtained four types of synoptically favorable environments for spring MCSs and two types of synoptically favorable environments for summer MCSs (types 1 and 2) using data for 2004–13. An important question is how well each type of synoptically favorable environment we identified can be used to estimate and explain the variability of MCS characteristics. Establishing the statistical relationship between the synoptically favorable environment and MCSs is useful for understanding the predictability of

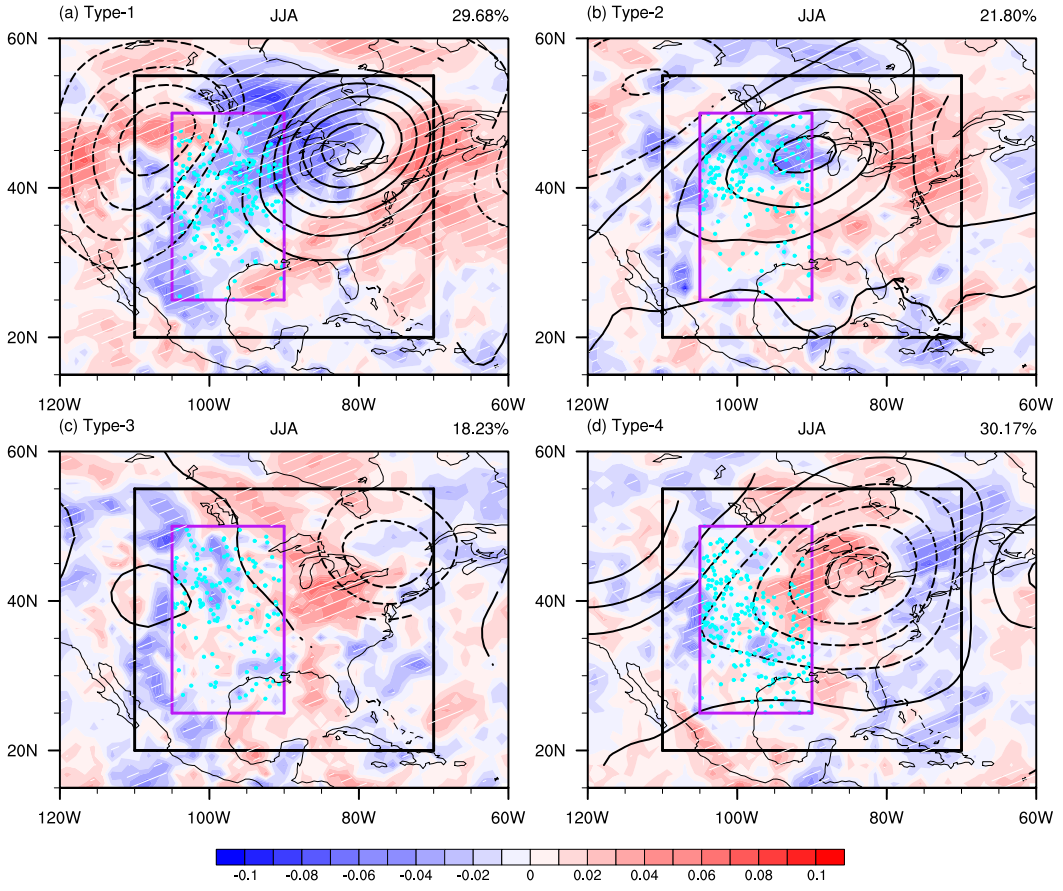

FIG. 8. As in Fig. 5, but for JJA.

MCSs and the implications for changes in the large-scale environment to MCS changes. Using 3 years of MCS-tracking data for 2014–16, we evaluate the explanatory power of each synoptically favorable environment type for estimating MCS occurrence and MCS characteristics. To achieve this goal, we developed a large-scale index (LI) based on pattern correlation between the large-scale environments of 2014–16 and the large-scale environment of the synoptically favorable types obtained from 2004–13 as follows:

$$\mathrm{LI} = \sum_{i=1}^{n} \mathrm{PCC}(i)N(i). \qquad (1)$$

Here, n is the total number of synoptically favorable types ($n = 4$ in spring and $n = 2$ in summer), i represents the type number, PCC(i) is the pattern correlation between the large-scale environments averaged over certain time intervals and those from type i, and $N(i)$ is the MCS property (i.e., MCS number, MCS precipitation rate, and MCS precipitation area) of type i averaged over the same time interval as PCC(i). The large-scale environments used here include zonal and meridional winds at three levels (925, 500, and 200 hPa) and specific humidity at two levels (925 and 200 hPa), the same as those used for the SOM analysis. We first normalized each variable over time, and then these variables for each node and the observed large-scale environments are mapped to a 1D array after spatial weighting, following the same procedure as used in the SOM analysis. We calculate LI using different time intervals (i.e., 3 h and 1, 1.5, 3, 6, and 12 days) for averaging the large-scale environments and the MCS properties to examine the sensitivity of the estimation to the time scale. Besides the large-scale environments, MCSs are influenced by other factors such as smaller-scale atmospheric and surface flux perturbations. We expect the large-scale environments to produce higher skill for longer averaging periods as the impacts of smaller-scale perturbations that are more stochastic in space and time tend to average out. In other words, while estimation of individual MCS events may require both large-scale environments and smaller-scale perturbations as precursors, the explanatory power of the mean large-scale

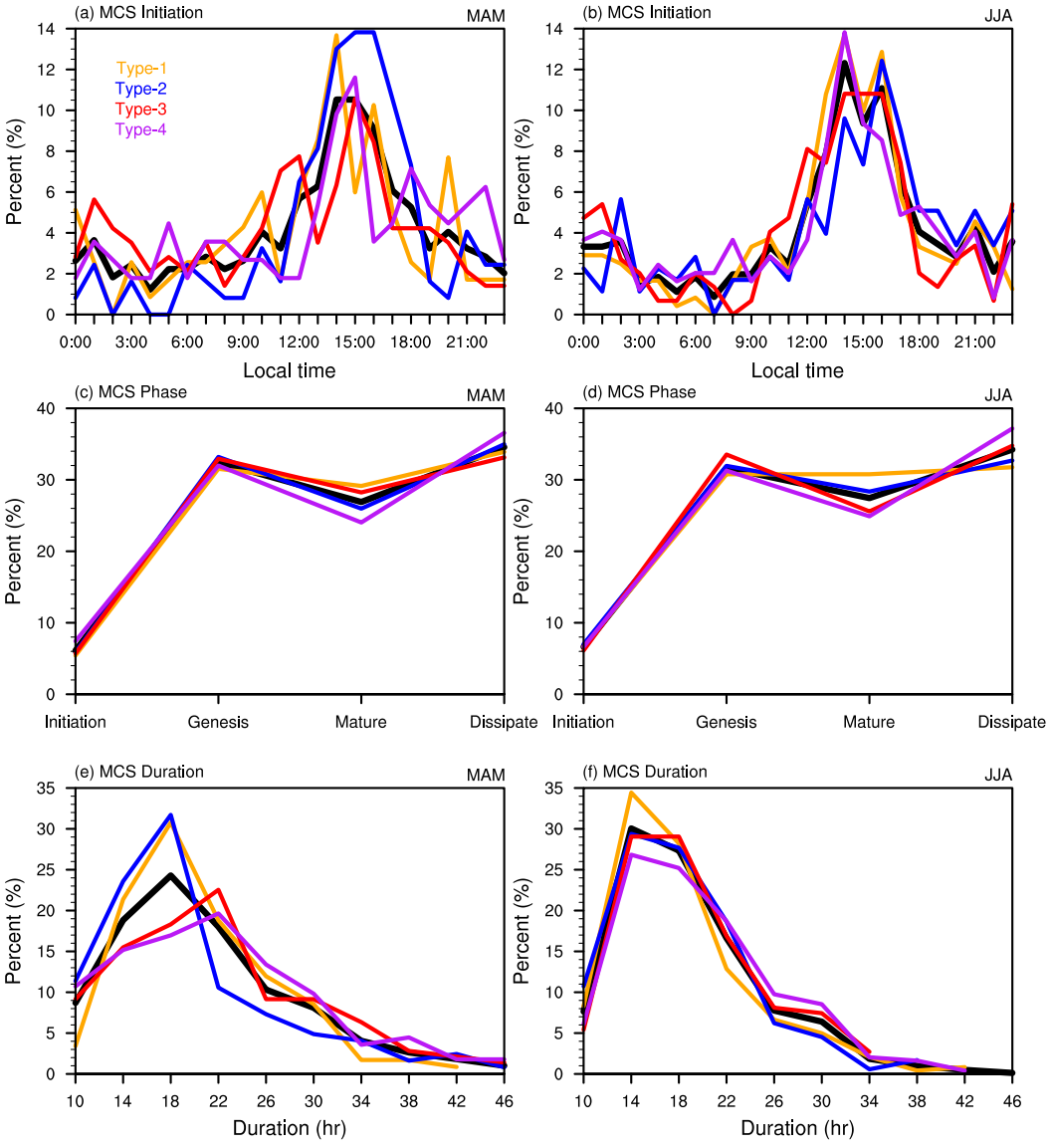

FIG. 9. Percentage of MCSs in each SOM type as a function of (a),(b) initiation times, (c),(d) life cycle stages, and (e),(f) duration during (left) MAM and (right) JJA. Black lines are for all MCSs while color lines are for MCSs for each SOM type.

environments for the mean MCS properties may increase over longer time periods.

Based on Eq. (1), we use LI to estimate the MCS number, precipitation rate, and precipitation area averaged every 3 days during spring and summer shown in Fig. 11. During spring, the large-scale index estimates the MCS number, precipitation rate, and precipitation area very well, with correlations of 0.50, 0.39, and 0.54, respectively, which are statistically significant at the 1% level based on the Student's t test. Note that here the MCS precipitation rate and precipitation area are calculated when there is at least one MCS in the domain. Hence, there are some missing values when there is no observed MCS in the domain. This way, we ensure that these three predictand variables are mostly independent, with near-zero correlation between each other. Since both precipitation rate and area are well predicted based on the large-scale environments, the precipitation amount is also well estimated, with a correlation of 0.50 in spring. During summer, the correlation decreases significantly, indicating the weakening role of the large-scale environments in MCS activity in the Great Plains. The correlation between the large-scale environments and MCS number, precipitation rate, and precipitation

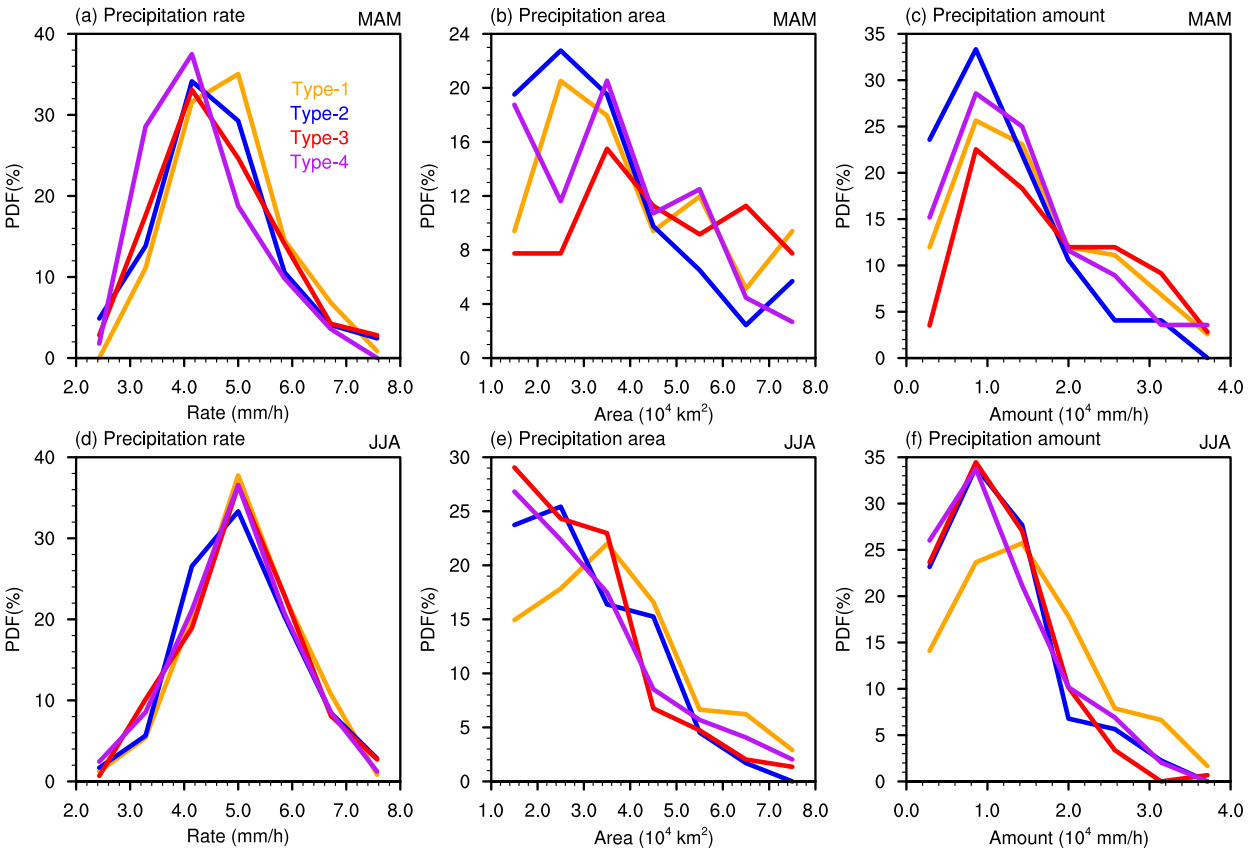

FIG. 10. Probability distribution function (PDF) of (a),(e) MCS precipitation rate (mm h^{-1}), (b),(f) MCS precipitation area (10^4 km^2), and (c),(g) MCS precipitation amount (10^4 mm h^{-1}) for each SOM type during (top) MAM and (bottom) JJA.

area is 0.21, 0.28 and 0.08, respectively. Except for precipitation area, the other two correlations are still significant at the 5% level, based on the Student's *t* test. The significantly lower correlations in summer mean that other smaller-scale forcings such as the midtropospheric perturbations (Wang et al. 2011a,b) embedded in the large-scale environments and/or surface flux perturbations may play a more important role in the predictability of MCSs. Note that we use different types of large-scale environment only based on the initiation moment of MCSs to predict MCS characteristics during the entire MCS duration to minimize the feedback of MCSs to the large-scale environments (e.g., Yang et al. 2017; Feng et al. 2018). When we use different types of large-scale environments based on all stages of the MCSs to estimate MCSs and their characteristics, the correlations between LI and MCS characteristics are much higher in both spring and summer. For example, the correlations between LI and MCS numbers in spring and summer reach 0.81 and 0.42 at 3-day intervals, respectively, significant at the 1% level based on the Student's *t* test. The increased skill when the large-scale environments during all MCS life cycle stages are included is consistent with the strong feedback of MCSs to the large-scale environments reported in previous studies.

Figure 12 displays the correlation between the estimated and actual MCS characteristics based on averaging at 12-day, 6-day, 3-day, 1.5-day, 1-day, and 3-h intervals. During spring, the correlation increases considerably as the averaging period increases, especially for MCS number and MCS precipitation rate. The correlation is 0.15 and 0.24 for MCS number and MCS precipitation rate, respectively, at 3-h intervals but it increases steadily to 0.57 and 0.61, respectively, at 12-day intervals. The correlation of MCS precipitation area also gradually increases from 0.41 at 3-h intervals to 0.58 at 12-day intervals. These results suggest that the large-scale environments provide more useful estimation of MCSs at longer time scale during spring. During summer, the correlation also increases with the time interval for MCS number and precipitation rate, with correlation increasing from 0.05 and 0.13 at 6-h intervals to 0.32 and 0.42 at 12-day intervals, respectively. Therefore,

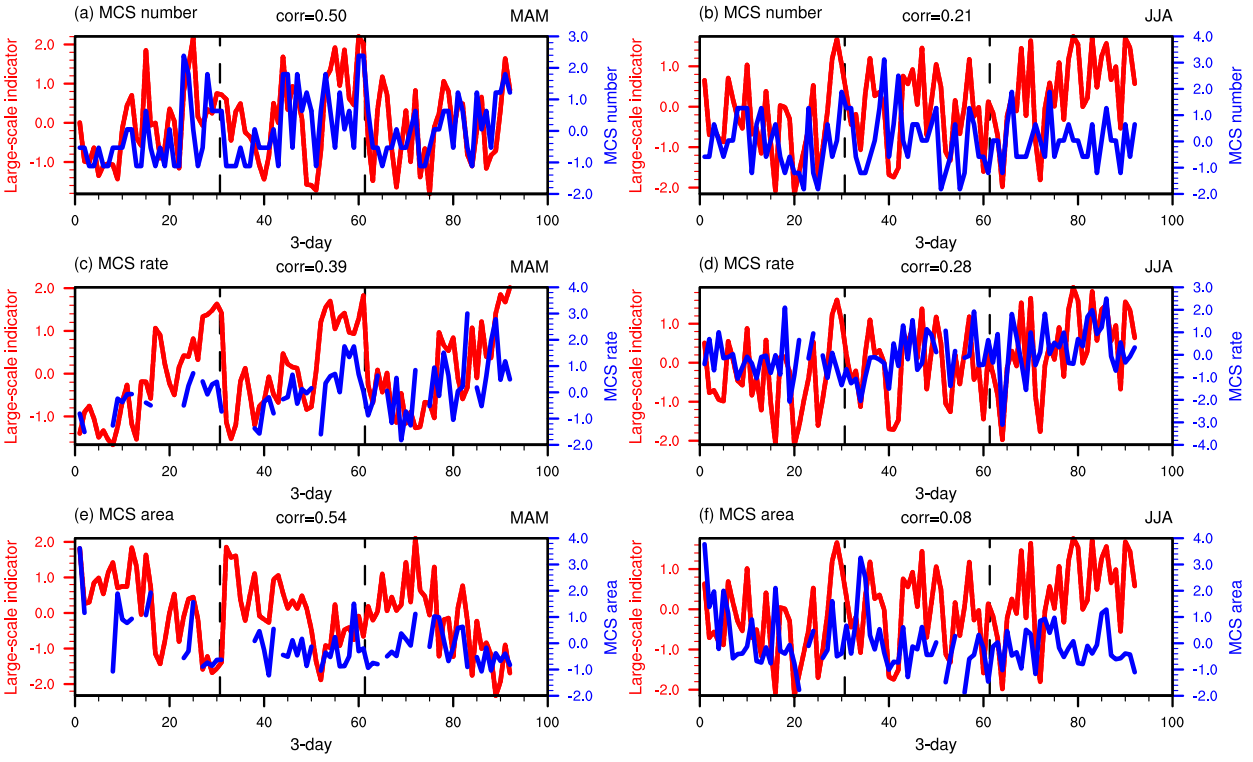

FIG. 11. Time series comparing LI (blue line) with observed (a),(b) MCS number (red line), (c),(d) MCS precipitation rate (red line), and (e),(f) MCS convective area (red line) at 3-day intervals and averaging during (left) MAM and (right) JJA from 2014 to 2016. All the time series are normalized. The two vertical dashed lines denote the first days of 2015 and 2016. Note that MCS precipitation rate and precipitation area when no MCS is observed are excluded in (c)–(f). The correlations (corr) between the large-scale index and MCS features are provided above each panel.

large-scale environments also exert increasing influence on the MCS number and precipitation rate at longer time scales during summer, albeit to a smaller extent compared to spring. For MCS precipitation area, the correlation remains almost unchanged from 3-h to 6-day intervals, and it almost vanishes at 12-day intervals. This consistently low skill suggests that summertime MCS precipitation area has almost no relationship with the large-scale environments. To examine the accuracy of the estimation, we also calculate the normalized root-mean-square-error (NRMSE) between the estimated and actual MCS features. The NRMSE is lower in spring than summer, indicating more accurate estimation in spring. With increased time interval, the NRMSE generally decreases, indicating more accurate estimation for longer-term averages.

4. Summary and conclusions

In this study, we identified four types of synoptically favorable environments for spring MCSs and two types of synoptically favorable environments and two types of synoptically unfavorable environments for summer MCSs over the Great Plains by conducting analysis using self-organizing map on North American Regional Reanalysis data and 10 years of MCSs tracked using observations (2004–13). During spring, two synoptically favorable environments are frontal systems and enhanced GPLLJ (Figs. 3 and 4). The former provides a lifting mechanism and the latter provides anomalous moisture for MCS development. There are two types of frontal environments (type 1 and type 3) and both of them feature an anomalous cyclone to the west and an anomalous anticyclone to the east of the Great Plains in the upper levels, favoring extensive midlevel upward motion over the Great Plains (Figs. 5a,c). The main difference between the two types is the more southward location of type 3 compared to type 1. Therefore, MCSs in type 3 are more concentrated over the southern Great Plains. Type 2 corresponds to an enhanced GPLLJ in the low levels (Figs. 3b and 4b) and an anticyclone in the upper level over the Great Plains (Fig. 5b). Hence, upward motion is favorable near the western boundary of the Great Plains, where most MCSs in this type are located. A weak low-level cyclone in the southern Great Plains is observed in type 4, with enhanced GPLLJ in the

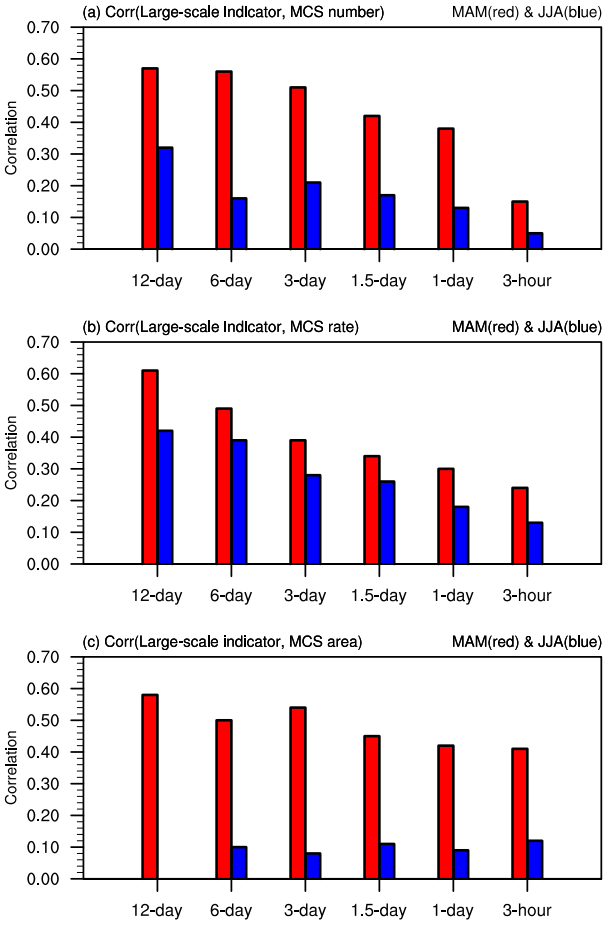

FIG. 12. Correlation between LI and (a) MCS number, (b) MCS precipitation rate, and (c) MCS convective area at different time intervals for MAM (red) and JJA (blue).

southern Great Plains (Figs. 3d and 4d). In the upper level, there is a cyclone to the west and an anticyclone to the east of the southern Great Plains, which favor upward motion and MCS initiation in the southern Great Plains (Fig. 5d).

During summer, the small positive CAPE and CIN anomalies when MCSs occur are quite different from the large positive CAPE and negative CIN anomalies during spring (Fig. 2). This finding suggests that even weak large-scale dynamical and thermodynamic perturbations may trigger MCSs in summer (Fig. 1). In other words, the MCS environments in summer may be either synoptically favorable or synoptically unfavorable. The two synoptically favorable types are also frontal situations (type 1; Figs. 6a–8a) and enhanced GPLLJ (type 2; Figs. 6b–8b), but with a more northward shift relative to spring. An enhanced upper-level ridge is observed in two types of the large-scale environments identified by SOM (type 3 and type 4; Figs. 6c and 6d). Such environments do not have synoptic-scale vertical air motion favorable for MCS development. With the abundance of mean-state moisture in summer, small-scale perturbations, too small to be evident on the synoptic scale, may generate upward motion sufficient to trigger MCSs. Therefore, for types 3 and 4, MCS initiation can occur even with small or even absent positive moisture anomalies on the synoptic scale (Figs. 7c,d).

Generally, MCSs initiate more frequently in the afternoon, with a maximum at ~1500 LT and a minimum at late night in both spring and summer (Figs. 9a,b). The MCSs for all four types show similar diurnal cycles, but MCSs for type 1 in spring, related to the enhanced GPLLJ, show larger diurnal cycle amplitude than the other types. MCSs spend the least amount of time in the initiation stage (~5%) and similar amounts of time in the other three stages (~25%–35%). The synoptic-front-related MCSs in spring and summer spend more time in the mature stage and less time in the dissipation stage than the other two types, suggesting that synoptic-scale forcing tends to support larger MCSs with more pronounced convective features and more expansive stratiform rain area (Figs. 9c,d). In spring, MCSs concentrated in the southern Great Plains (type 3 and type 4) often last longer than MCSs concentrated in the northern Great Plains (type 1 and type 2) (Fig. 9e), which may be related to the meridional gradient of CAPE (Fig. 2e). In summer, the non-synoptic-related MCSs (types 3 and 4) often last longer than the synoptic-related MCSs (types 1 and 2), especially for type 4 (Fig. 9f). The MCS precipitation rate, precipitation area, and precipitation amount are much larger in frontal-related MCSs in spring and summer than the other types, which may be due to higher and more spatially extensive moisture anomalies and stronger lifting in these types (Fig. 10).

We have constructed a large-scale index (LI) based on the pattern correlation between the large-scale environments at certain time intervals during 2014–16 and the synoptically favorable types (all four types in spring and the first two types in summer) obtained based on training of the SOM using NARR and MCSs data for 2004–13. LI calculated at 3-day interval predicts the MCS number, precipitation rate, and precipitation area with high skill during spring, with correlation of 0.50, 0.39, and 0.54 for MCS number, precipitation rate, and precipitation area, respectively. However, the prediction skill is low during summer, with correlations of 0.21, 0.28, and 0.08 for MCS number, precipitation rate, and precipitation area, respectively. The correlation increases with longer time interval and averaging period with the correlations during spring increasing from 0.15,

0.24, and 0.41 for MCS number, precipitation rate, and area, respectively, at 3-h intervals to 0.57, 0.61, and 0.58, respectively, at 12-day intervals. During summer, the correlations are quite weak at 3-h intervals, at only 0.05, 0.13, and 0.12 for MCS number, precipitation rate, and area, respectively. The correlations for MCS number and precipitation rate increase gradually to 0.32 and 0.42 respectively at 12-day intervals. These results indicate that the large-scale environment tends to exert larger influence on the MCSs at longer time scales (6 or 12 days), while other factors (e.g., surface fluxes, mid-tropospheric perturbation) become much less important due to their inherent shorter time/space scales. It should be noted that even at a 6- or 12-day interval, MCS variance explained by the large-scale environment is rather small during summer, suggesting the need to better understand what limits the predictability of summer MCSs in the future.

Because of the coarse resolution and limitations in various physical parameterizations, current global climate models mostly fail to simulate MCSs, thus limiting their ability to simulate the precipitation and surface temperature in the U.S. Great Plains and their diurnal variability (Gao et al. 2017; Lin et al. 2017; van Weverberg et al. 2018). Analyses of the type presented here, based on observations, can be extended to climate modeling to evaluate how well current climate models simulate the MCS-favorable large-scale environments and to understand what aspects of the various environment types may be deficient in model simulations and the reasons for the biases. Knowledge of the relationship between the large-scale environments and MCS occurrence and characteristics also provides a key foundation for understanding how changes in the large-scale environments may influence MCSs and their properties in the future.

Acknowledgments. This research is supported by the U.S. Department of Energy Office of Science Biological and Environmental Research as part of the Regional and Global Modeling and Analysis program. PNNL is operated for the Department of Energy by Battelle Memorial Institute under Contract DE-AC05-76RL01830. Robert A. Houze was supported by master agreement 243766 between the University of Washington and PNNL. The Global Merged IR dataset is obtained at NASA Goddard Earth Sciences Data and Information Services Center (https://dx.doi.org/10.5067/P4HZB9N27EKU), the GridRad radar dataset is obtained at the Research Data Archive of the National Center for Atmospheric Research (NCAR) (https://rda.ucar.edu/datasets/ds841.0/), the StageIV data are obtained at the NCAR Earth Observing Laboratory (https://data.eol.ucar.edu/dataset/21.093), and the NARR dataset is obtained at NOAA Earth System Research Laboratory Physical Science Division (https://www.esrl.noaa.gov/psd/data/narr/).

REFERENCES

Anderson, C. J., and R. W. Arritt, 1998: Mesoscale convective complexes and persistent elongated convective systems over the United States during 1992 and 1993. *Mon. Wea. Rev.*, **126**, 578–599, https://doi.org/10.1175/1520-0493(1998)126<0578:MCCAPE>2.0.CO;2.

Augustine, J. A., and K. W. Howard, 1991: Mesoscale convective complexes over the United States during 1986 and 1987. *Mon. Wea. Rev.*, **119**, 1575–1589, https://doi.org/10.1175/1520-0493(1991)119<1575:MCCOTU>2.0.CO;2.

Bao, M., and J. M. Wallace, 2015: Cluster analysis of Northern Hemisphere wintertime 500-hPa flow regimes during 1920–2014. *J. Atmos. Sci.*, **72**, 3597–3608, https://doi.org/10.1175/JAS-D-15-0001.1.

Coniglio, M. C., D. J. Stensrud, and M. B. Richman, 2004: An observational study of derecho-producing convective systems. *Wea. Forecasting*, **19**, 320–337, https://doi.org/10.1175/1520-0434(2004)019<0320:AOSODC>2.0.CO;2.

——, J. Y. Hwang, and D. J. Stensrud, 2010: Environmental factors in the upscale growth and longevity of MCSs derived from rapid update cycle analyses. *Mon. Wea. Rev.*, **138**, 3514–3539, https://doi.org/10.1175/2010MWR3233.1; Corrigendum, **139**, 2686–2688, https://doi.org/10.1175/MWR-D-11-00064.1.

Cooney, J. W., K. P. Bowman, C. R. Homeyer, and T. M. Fenske, 2018: Ten-year analysis of tropopause-overshooting convection using GridRad data. *J. Geophys. Res. Atmos.*, **123**, 329–343, https://doi.org/10.1002/2017JD027718.

Dee, D. P., and Coauthors, 2011: The ERA-Interim Reanalysis: Configuration and performance of the data assimilation system. *Quart. J. Roy. Meteor. Soc.*, **137**, 553–597, https://doi.org/10.1002/qj.828.

Feng, Z., L. R. Leung, S. Hagos, R. A. Houze, C. D. Burleyson, and K. Balaguru, 2016: More frequent intense and long-lived storms dominate the springtime trend in central US rainfall. *Nat. Commun.*, **7**, 13429, https://doi.org/10.1038/ncomms13429.

——, ——, R. A. Houze, S. Hagos, J. Hardin, Q. Yang, B. Han, and J. Fan, 2018: Structure and evolution of mesoscale convective systems: Sensitivity to cloud microphysics in convection-permitting simulations over the United States. *J. Adv. Model. Earth Syst.*, **10**, 1470–1494, https://doi.org/10.1029/2018MS001305.

——, R. A. Houze, R. Leung, F. Song, J. Hardin, J. Wang, W. I. Gustafson Jr., and C. R. Homeyer, 2019: Spatiotemporal characteristics and large-scale environments of mesoscale convective systems east of the Rocky Mountains. *J. Climate*, https://doi.org/10.1175/JCLI-D-19-0137.1, in press.

Fritsch, J. M., and R. A. Maddox, 1981: Convectively driven mesoscale weather systems aloft. Part I: Observations. *J. Appl. Meteor.*, **20**, 9–19, https://doi.org/10.1175/1520-0450(1981)020<0009:CDMWSA>2.0.CO;2.

——, and G. S. Forbes, 2001: Mesoscale convective systems. *Severe Convective Storms, Meteor. Monogr.*, No. 50, Amer. Meteor. Soc., 323–358, https://doi.org/10.1175/0065-9401-28.50.323.

——, R. J. Kane, and C. R. Chelius, 1986: The contribution of mesoscale convective weather systems to the warm-season precipitation in the United States. *J. Appl. Meteor. Climatol.*,

25, 1333–1345, https://doi.org/10.1175/1520-0450(1986)025<1333:TCOMCW>2.0.CO;2.

——, J. D. Murphy, and J. S. Kain, 1994: Warm core vortex amplification over land. *J. Atmos. Sci.*, **51**, 1780–1807, https://doi.org/10.1175/1520-0469(1994)051<1780:WCVAOL>2.0.CO;2.

Gao, Y., L. R. Leung, C. Zhao, and S. Hagos, 2017: Sensitivity of summer precipitation to model resolution and convective parameterizations across gray zone resolutions. *J. Geophys. Res. Atmos.*, **122**, 2714–2733, https://doi.org/10.1002/2016JD025896.

Gensini, V. A., T. L. Mote, and H. E. Brooks, 2014: Severe-thunderstorm reanalysis environments and collocated radiosonde observations. *J. Appl. Meteor. Climatol.*, **53**, 742–751, https://doi.org/10.1175/JAMC-D-13-0263.1.

Haberlie, A. M. and W. S. Ashley, 2019: A radar-based climatology of mesoscale convective systems in the United States. *J. Climate*, **32**, 1591–1606, https://doi.org/10.1175/JCLI-D-18-0559.1.

Hoch, J., and P. Markowski, 2005: A climatology of springtime dryline position in the U.S. Great Plains region. *J. Climate*, **18**, 2132–2137, https://doi.org/10.1175/JCLI3392.1.

Homeyer, C. R., and K. P. Bowman, 2017: Algorithm description document for version 3.1 of the three-dimensional gridded NEXRAD WSR-88D radar (GridRad) dataset. Tech. rep., 23 pp., http://gridrad.org/pdf/GridRad-v3.1-Algorithm-Description.pdf.

Houze, R. A., Jr., 2004: Mesoscale convective systems. *Rev. Geophys.*, **42**, RG4003, https://doi.org/10.1029/2004RG000150.

——, 2018: 100 years of research on mesoscale convective systems. *A Century of Progress in Atmospheric and Related Sciences: Celebrating the American Meteorological Society Centennial*, *Meteor. Monogr.*, No. 59, Amer. Metor. Soc., 17.1–17.54, https://doi.org/10.1175/AMSMONOGRAPHS-D-18-0001.1.

Janowiak, J., B. Joyce, and P. Xie, 2017: NCEP/CPC L3 Half Hourly 4km Global (60°S–60°N) Merged IR V1. A. Savtchenko, Ed., Goddard Earth Sciences Data and Information Services Center (GES DISC), Accessed 1 February 2018, https://doi.org/10.5067/P4HZB9N27EKU.

Johns, R. H., 1982: A synoptic climatology of northwest-flow severe weather outbreaks. Part I: Nature and significance. *Mon. Wea. Rev.*, **110**, 1653–1663, https://doi.org/10.1175/1520-0493(1982)110<1653:ASCONF>2.0.CO;2.

——, 1984: A synoptic climatology of northwest-flow severe weather outbreaks. Part II: Meteorological parameters and synoptic patterns. *Mon. Wea. Rev.*, **112**, 449–464, https://doi.org/10.1175/1520-0493(1984)112<0449:ASCONF>2.0.CO;2.

——, 1993: Meteorological conditions associated with bow echo development in convective storms. *Wea. Forecasting*, **8**, 294–299, https://doi.org/10.1175/1520-0434(1993)008<0294:MCAWBE>2.0.CO;2.

Keyser, D. A., and D. R. Johnson, 1984: Effects of diabatic heating on the ageostrophic circulation of an upper tropospheric jet streak. *Mon. Wea. Rev.*, **112**, 1709–1724, https://doi.org/10.1175/1520-0493(1984)112<1709:EODHOT>2.0.CO;2.

King, A. T., and A. D. Kennedy, 2019: North American supercell environments in atmospheric reanalysis and RUC-2. *J. Appl. Meteor. Climatol.*, **58**, 71–92, https://doi.org/10.1175/JAMC-D-18-0015.1.

Kohonen, T., 2001: *Self-Organizing Maps*. Springer, 502 pp.

Lee, S., T. Gong, N. Johnson, S. B. Feldstein, and D. Pollard, 2011: On the possible link between tropical convection and the Northern Hemisphere Arctic surface air temperature change between 1958 and 2001. *J. Climate*, **24**, 4350–4367, https://doi.org/10.1175/2011JCLI4003.1.

Lin, Y., 2011: GCIP/EOP Surface: Precipitation NCEP/EMC 4KM Gridded Data (GRIB) Stage IV Data. Version 1.0. UCAR/NCAR, Earth Observing Laboratory, Accessed November 2017, https://doi.org/10.5065/D6PG1QDD.

——, W. Dong, M. Zhang, Y. Xie, W. Xue, J. Huang, and Y. Luo, 2017: Causes of model dry and warm bias over central U.S. and impact on climate projections. *Nat. Commun.*, **8**, 881, https://doi.org/10.1038/s41467-017-01040-2.

Maddox, R. A., 1980: Mesoscale convective complexes. *Bull. Amer. Meteor. Soc.*, **61**, 1374–1387, https://doi.org/10.1175/1520-0477(1980)061<1374:MCC>2.0.CO;2.

——, 1983: Large-scale meteorological conditions associated with midlatitude, mesoscale convective complexes. *Mon. Wea. Rev.*, **111**, 1475–1493, https://doi.org/10.1175/1520-0493(1983)111<1475:LSMCAW>2.0.CO;2.

——, C. F. Chappell, and L. R. Hoxit, 1979: Synoptic and meso-α-scale aspects of flash flood events. *Bull. Amer. Meteor. Soc.*, **60**, 115–123, https://doi.org/10.1175/1520-0477-60.2.115.

Mesinger, F., and Coauthors, 2006: North American Regional Reanalysis. *Bull. Amer. Meteor. Soc.*, **87**, 343–360, https://doi.org/10.1175/BAMS-87-3-343.

Nesbitt, S. W., R. Cifelli, and S. A. Rutledge, 2006: Storm morphology and rainfall characteristics of TRMM precipitation features. *Mon. Wea. Rev.*, **134**, 2702–2721, https://doi.org/10.1175/MWR3200.1.

Ninomiya, K., 1971: Mesoscale modification of synoptic situations from thunderstorm development as revealed by ATS III and aerological data. *J. Appl. Meteor.*, **10**, 1103–1121, https://doi.org/10.1175/1520-0450(1971)010<1103:MMOSSF>2.0.CO;2.

Perkey, D. J., and R. A. Maddox, 1985: A numerical investigation of a mesoscale convective system. *Mon. Wea. Rev.*, **113**, 553–566, https://doi.org/10.1175/1520-0493(1985)113<0553:ANIOAM>2.0.CO;2.

Peters, J. M., and R. S. Schumacher, 2014: Objective categorization of heavy-rain-producing MCS synoptic types by rotated principal component analysis. *Mon. Wea. Rev.*, **142**, 1716–1737, https://doi.org/10.1175/MWR-D-13-00295.1.

Pokharel, B., S. Y. Wang, J. Meyer, R. Gillies, and Y. Lin, 2019: Climate of the weakly-forced yet high-impact convective storms throughout the Ohio River Valley and Mid-Atlantic United States. *Climate Dyn.*, **52**, 5709–5721, https://doi.org/10.1007/S00382-018-4472-0.

Reusch, D. B., R. B. Alley, and B. C. Hewitson, 2007: North Atlantic climate variability from a self-organizing map perspective. *J. Geophys. Res.*, **112**, D02104, https://doi.org/10.1029/2006JD007460.

Schumacher, R. S., and R. H. Johnson, 2005: Organization and environmental properties of extreme-rain-producing mesoscale convective systems. *Mon. Wea. Rev.*, **133**, 961–976, https://doi.org/10.1175/MWR2899.1.

——, and ——, 2006: Characteristics of U.S. extreme rain events during 1999–2003. *Wea. Forecasting*, **21**, 69–85, https://doi.org/10.1175/WAF900.1.

Smull, B. F., and J. A. Augustine, 1993: Multiscale analysis of a mature mesoscale convective complex. *Mon. Wea. Rev.*, **121**, 103–132, https://doi.org/10.1175/1520-0493(1993)121<0103:MAOAMM>2.0.CO;2.

Stensrud, D. J., 1996: Effects of a persistent, midlatitude mesoscale region of convection on the large-scale environment during the warm season. *J. Atmos. Sci.*, **53**, 3503–3527, https://doi.org/10.1175/1520-0469(1996)053<3503:EOPMMR>2.0.CO;2.

Van Weverberg, K., and Coauthors, 2018: CAUSES: Attribution of surface radiation biases in NWP and climate models near the U.S. Southern Great Plains. *J. Geophys. Res. Atmos.*, **123**, 3612–3644, https://doi.org/10.1002/2017JD027188.

Wang, J., X. Dong, A. Kennedy, B. Hagenhoff, and B. Xi, 2019: A regime-based evaluation of southern and northern Great Plains warm-season precipitation events in WRF. *Wea. Forecasting*, **34**, 805–831, https://doi.org/10.1175/waf-d-19-0025.1.

Wang, S.-Y., T.-C. Chen, and J. Correia, 2011a: Climatology of summer midtropospheric perturbations in the US northern plains. Part I: Influence on northwest flow severe weather outbreaks. *Climate Dyn.*, **36**, 793–810, https://doi.org/10.1007/s00382-009-0696-3.

——, ——, and E. S. Takle, 2011b: Climatology of summer midtropospheric perturbations in the US northern plains. Part II: Large-scale effects of the Rocky Mountains on genesis. *Climate Dyn.*, **36**, 1221–1237, https://doi.org/10.1007/s00382-010-0765-7.

Wolf, B. J., and D. R. Johnson, 1995: The mesoscale forcing of a midlatitude upper-tropospheric jet streak by a simulated convective system. Part I: Mass circulation and ageostrophic processes. *Mon. Wea. Rev.*, **123**, 1059–1087, https://doi.org/10.1175/1520-0493(1995)123<1059:TMFOAM>2.0.CO;2.

Yang, Q., R. A. Houze Jr., L. R. Leung, and Z. Feng, 2017: Environments of long-lived mesoscale convective systems over the central United States in convection permitting climate simulations. *J. Geophys. Res.*, **122**, 13 288–13 307, https://doi.org/10.1002/2017JD027033.

Zipser, E. J., 1982: Use of a conceptual model of the life cycle of mesoscale convective systems to improve very-short-range forecasts. *Nowcasting*, K. Browning, Ed., Academic Press, 191–221.